Supplementary Materials for

# Seismic evidence for continental subduction beneath the Western Alps

Liang Zhao*, Anne Paul, Stéphane Guillot, Stefano Solarino, Marco G. Malusà,

Tianyu Zheng, Coralie Aubert, Simone Salimbeni, Thierry Dumont

Stéphane Schwartz, Rixiang Zhu, Qingchen Wang

This PDF file includes

Materials and Methods (S1 to S5)

Figs. S1 to S6

References (25-41)

## S1 Data, computation of receiver functions and quality control

The CIFALPS project (China-Italy-France Alps seismic survey) was the first passive seismic transect with dense station spacing in the western Alps. Forty-six temporary broadband seismic stations (Fig. 1) were deployed along the WSW-ENE transect with spacing from 5 km in the central part where the ECORS-CROP reflection profile failed to image the European Moho (*11*), to 10 km at both ends. Stations were operated from July 2012 to September 2013. Special care was taken in the site survey and installation to ensure data quality, in particular in the Po Plain.

A radial (or transverse) receiver function (*25*) is computed for each 3-component record of a distant earthquake by deconvolution of the vertical component from the radial (or transverse). This processing removes the earthquake source signature and travel path effects from the source to beneath the recording station. The time delay between the converted P to S waves and the direct P wave is proportional to the depth of the converting interface and the average velocity structure above it.

For calculation of receiver functions, we selected events with magnitude $\geq 5.5$ and epicentral distance between 30º and 90º. Three-component recordings of distant earthquakes were bandpass filtered (two-pole Butterworth filter) between 0.05 and 0.8 Hz androtated into the local Z-R-T ray-based coordinate system. We then checked data quality by computing the signal-to-noise ratio (SNR) as the ratio of the peak amplitude of the P phase to the average amplitude across an 8 s time window prior to the onset of the P phase. All P records with SNR$< 2$ on the radial component were excluded from further analysis. A first turn of visual inspection was then performed to

remove remaining low-quality records.

Radial and transverse receiver functions were computed using the time domain iterative deconvolution method (*26*). A second turn of visual inspection was performed to remove low-quality receiver functions. As a result, 84 events (Fig. S1) contributed 1647 radial receiver functions.

Figure S2 shows radial RF selected for events with ENE backazimuths (see text S3), stacked by station, and plotted along the reference profile (see text S2).

## S2 Depth migration of receiver functions

To produce a depth image beneath the receiver array, we migrated time section to depth and stacked the radial receiver functions using the common conversion point method (*27*). Provided that an appropriate migration velocity model is used, Ps conversions delineate layer boundaries on the migrated depth section. The 3-D model space beneath the array was subdivided into a three-dimensional grid of cells.Then, the radial receiver functions were back-projected from the receiver to the source through these cells with constant ray parameters, assuming a modified IASP91 standard Earth model (*28*) with laterally variable crustal P-wave velocity along the array. The amplitude of each cell was obtained by averaging amplitudes of the radial receiver function of the crossing ray paths, that is by assigning each P to S conversion to the location that generated it assuming a flat-layered velocity model beneath each station. Finally, cells located out of the average profile (trending 73º with middle point at 6.6ºE , 44.7ºN; Fig. 1) were projected orthogonally onto the profile and stacked.

The velocity model used for time-to-depth migration was constructed based upon a number of previous works. The profile was divided into 4 segments with different 1-D migration velocity models (Table S1). The Vp/Vs ratio was set to 1.73 in all layers. Although dipping interfaces are usually shifted to shallower position with the CCP method, synthetic migration tests (*6*) showed that for dipping angle smaller than 30° (which is the case in this study), the shift is negligible. This is confirmed by our 2D synthetic modelling (S5).

## S3 Effect of event backazimuth on the CCP section

The waveforms of the radial receiver functions strongly depend on event backazimuth, yielding different CCP images for different ranges of backazimuth, as shown by Fig. S3. This is due to departures from the 1-D velocity structure assumption that underlies the CCP migration method. Fig. S3 however shows that the main features of the CCP section (European Moho, "inverted Moho" of the suture zone) are well retrieved in the two ranges of backazimuth that include a significant number of events (NNW and ENE). Salient differences appear for the converted phases from the Adriatic Moho that change geometry and depth with backazimuth. The image of this structure may however also be altered by lower signal-to-noise ratio than in other parts of the profile.

Cassidy (*29*) showed that dipping interfaces generate stronger converted phases for events with updip incidences. As most geological structures have east to northeastward dips, we decided to display the CCP section computed from events with ENE backazimuths (28º-118º) in the main text. This is also the best option to

attenuate out-of-plane diffracted signals due to 3-D structure. Finally, this selection of events in the direction of the profile is more appropriate for comparison with the results of 2-D synthetic seismograms.

## S4 Building and testing the density/velocity interpretative model

The CCP depth section provided basic elements on the geometry of the main layer boundaries and velocity contrasts (European Moho, top of Ivrea body, "inverted Moho"). Additional data on the crustal structure available along our profile and in neighbouring regions were used to better constrain the geometry of possible 2-D models including controlled-source seismic data (*10*), depth to European Moho from the wide-angle data (*30*), geometry of top of Ivrea body (*31*, *32*), basement depth in the France Southeast basin (*33*), and in the Po plain (*34*).The geological input to the final interpretative model, especially the positions where known metamorphisms outcrop on the surface, was also considered.

The P-to-S conversions on the Adriatic Moho have strong amplitudes, but they are laterally discontinuous and their geometry and depth strongly depend on backazimuth (see Fig. S3). Moreover, the 10 km Moho jump that comes out at x=140 km in the CCP section (Fig. 2c) is hardly compatible with the slowly decreasing Bouguer anomaly (Fig. 2a). Thereafter, we decided to assume a smooth Adriatic Moho at a depth rising from 32 km at the eastern end of the profile to 9 km at x=75 km on top of the Ivrea body. We set the maximum depth of the Adriatic Moho at 30-32 km according to the MAMBo velocity model developed for the Po plain (*34*). We used the same source of information to set the depth of the other layer boundaries,

basement and top of lower crust that are not imaged by the receiver function data.

In the western part of the profile, we used the map of the top of the basement in the France Southeast basin (*33*). The geometry of the basement was later modified to fit the Bouguer anomaly. The lower crustal thickness was set according to the ECORS-CROP deep seismic reflection data recorded in the northwestern Alps (*11*). The picked European Moho fits the Moho depth estimates (*30*) from wide-angle reflection data in the [-75 km, 20 km] part of our profile.

In the internal Alps, we built our crustal model based on the results of: 1) the 1958-1960 seismic experiments of the western Alps (*13*), 2) the local earthquake tomography (*31*) complemented by the sequential inversion of local earthquake traveltimes and gravity anomaly (*32*). Since Closs and Labrouste (*13*), we know that the shallowest part of the "Ivrea surface" (top surface of the Ivrea body) is located at 10 km depth, 10-20 km west of the city of Torino, that is at x=70-80 km along our profile. At this depth, the measured Vp in the Ivrea body was 7.4 $km.s^{-1}$. The shape of the Ivrea body of our model mimics the shape of the high velocity - high density body imaged (*32*) along an E-W profile located slightly south of our array. To account for a likely velocity increase with depth in the Ivrea body (due to a likely decrease in the volume ratio of serpentinite to peridotite), we divided the body into 2 parts at an arbitrary depth of 17 km. The lower boundary of the Ivrea body, which corresponds to the transition from serpentinized peridotite to peridotite, was set at 30 km depth. This is both the depth of the Adriatic Moho to the NNE and the average depth of the "inverted Moho" in the CCP section to the WSW.

After constructing the model geometry, we checked its compatibility with the Bouguer anomaly data by gravity modelling. We used the forward method (*35*) to compute the gravity field induced at the surface by a 2-D model made of polygons of arbitrary density and shape. The observed gravity anomaly is computed from the WGM2012 global gravity model (*18*). We extracted Bouguer anomaly data in a 30-km wide strip following the seismic array and we projected the data points onto the reference profile. This provided us with an average Bouguer anomaly curve with error estimates (Fig. 2a and S4). We then used gravity modeling to find the set of density values that fit the observed anomaly the best. The final density model and the computed and observed Bouguer anomalies are showed on Fig. S4.

## S5 Two-dimensional integrated forward modelling of the CCP section

We performed a series of 2-D synthetic tests in order to test our interpretation of the CCP section (which fits the Bouguer anomaly data). We focus on the modelling of the broad blue spot of negative-polarity P-to-S converted phases beneath the Dora Maira massif, and on the hypothesis of subduction of the European lower crust in the Adriatic mantle. As we don't focus on shallow structures, we combined the results of previous studied for the shallow sediment layers (see S4).

Synthetic seismograms were first computed for different lithospheric structures using a 2-D hybrid numerical method (Fig. S5) (*36*, *37*). The PREM model was used as background model (*38*). The crustal model along the CIFALPS profile is embedded in a 1000 km × 430 km box, inside which we used the spectral element method (*39*), and outside which we used the generalized ray theory (*40*). Vertical and radial

components of synthetic seismograms were calculated for 10 events at teleseismic distance mimicking the distribution of events used in the CCP section, that is with epicentral distance ranging from ~30 to 90º. In a second step, we estimated radial receiver functions and produced a CCP image using exactly the same deconvolution method, filters and migration method and parameters as those used for the observed dataset.

We computed CCP sections for crustal density models that fit the observed gravity anomaly. Density values were converted to P wave velocity values using different empirical or experimental density-velocity relationships: the empirical linear relationship for the sediment layers (Vp=3.85$\rho$-4.81 with Vp in km·s$^{-1}$ and $\rho$ in $10^3$ kg·m$^3$)(*41*), relationship for the upper and lower crust (*42*, *43*), experiment data for the Ivrea body and mantle layer in subduction zones (*23*, *44*).The Vp/Vs ratio was set to 1.73 in all layers. It is worthy to note that, in the suture zone, a correct fit to the observed gravity anomaly requires separating the body in 2 parts, with Vp=7.4 km·s$^{-1}$, $\rho$=2900 kg·m$^{-3}$ in the upper part (peridotite with 60% serpentinite) and Vp=7.9 km·s$^{-1}$, $\rho$=3100 kg·m$^{-3}$ in the lower part (peridotite with 30% serpentinite), in the space between the bottom of the Ivrea body and the top of the subducted lower crust, the fit to the seismic data requires Vp<7.9 km·s$^{-1}$ (*23*). This layer may be peridotite with 45% of serpentinite.

For comparison, another model with a homogeneous high-velocity mantle wedge has been tested (Fig. S6). As expected, the corresponding CCP image displays a negative signal of limited east-west extension on top and parallel to the European

Moho positive conversion, much closer to the image of continental subduction in the Pamir (*6*) than to our image of the West-alpine continental subduction.

Table S1. Crustal velocity model used for time-to-depth migration of the receiver functions. The unit of Vpis in $km.s^{-1}$, and thickness (h) in km. The first velocity model corresponds to the Southeast basin, the second one to the external Alps, the third one to the internal Alps, and the fourth one to the Po basin.

| Layers | -150 to -50km | | -50 to 15km | | 15 to 80 km | | 80 to 165 km | |
|---|---|---|---|---|---|---|---|---|
| | Vp | h | Vp | h | Vp | h | Vp | h |
| 1st layer | 5.0 | 5 | 5.5 | 2 | 5.5 | 2 | 4.1 | 10 |
| 2nd layer | 6.0 | 15 | 6.1 | 18 | 5.8 | 10 | 6.0 | 11 |
| 3rd layer | 6.8 | 25 | 6.8 | 35 | 7.2 | 24 | 6.8 | 24 |
| 4th layer | - | - | - | - | 6.8 | 44 | - | - |

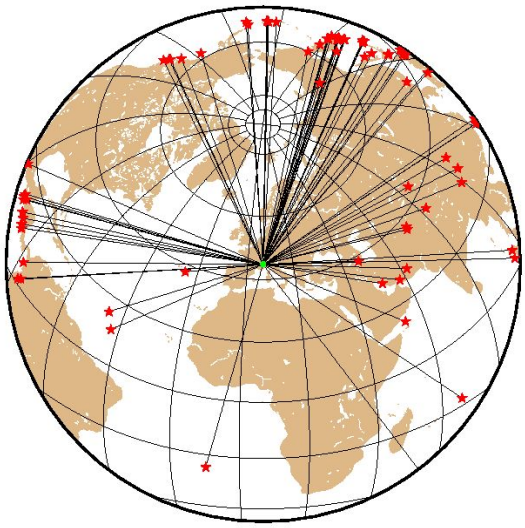

Figure S1. Locations of events (red stars) used in the receiver function analysis. The green square shows the location of the study area. Most events have NNW to E back-azimuths.

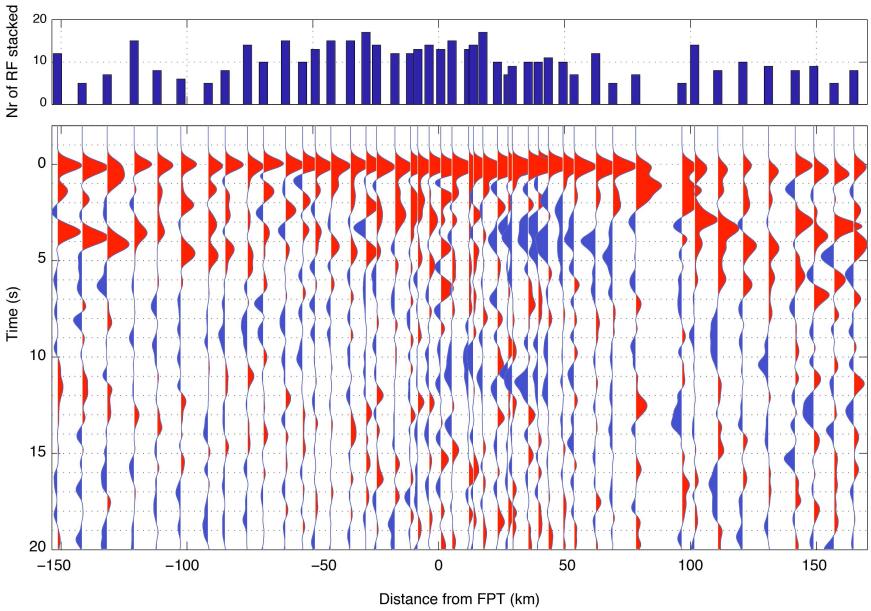


Figure S2. Time traces of radial receiver function stacked by station and plotted at the location of the station along the reference profile (bottom). We only stacked receiver function corresponding to ENE (28-118°) back-azimuths. The number of individual receiver function stacked for each station is displayed in the bar plot (top).

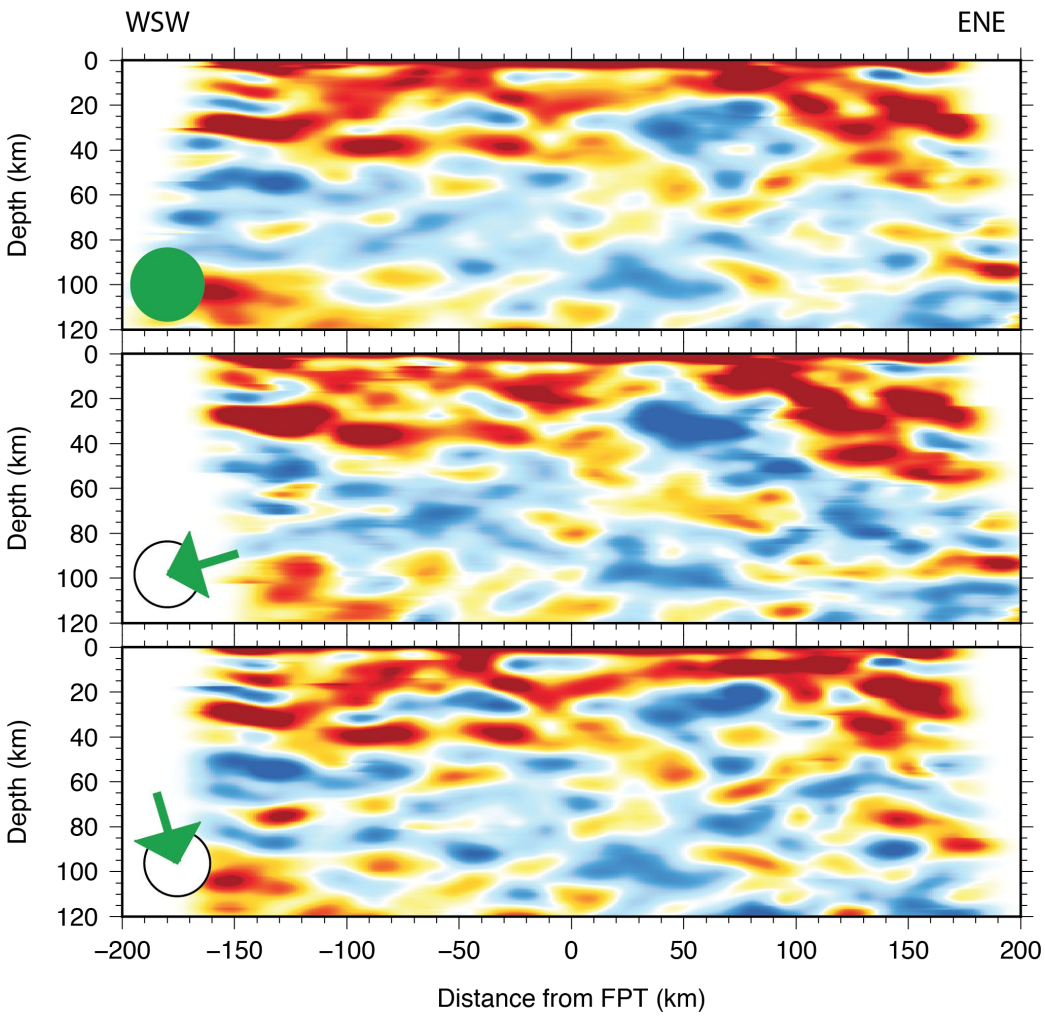


Figure S3. CCP depth sections computed for events in different ranges of backazimuth: all backazimuths (top); ENE backazimuths (28°-118°; middle); NNW backazimuths (298°-28°; bottom).

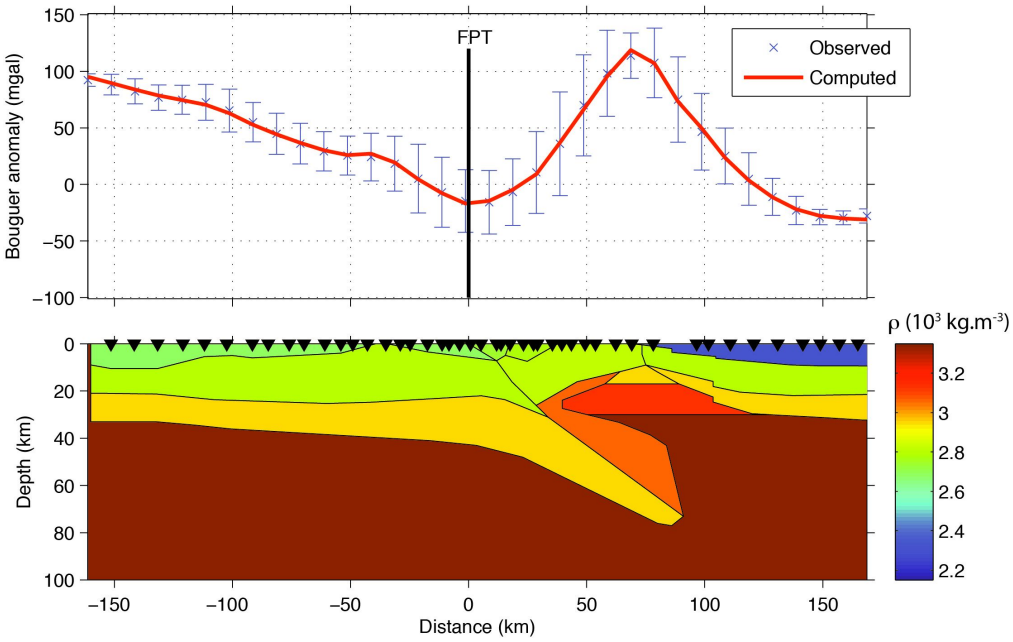


Figure S4. Best-fitting gravity model (bottom), with observed (blue markers with error bars) and computed (red curve) gravity anomalies (top).

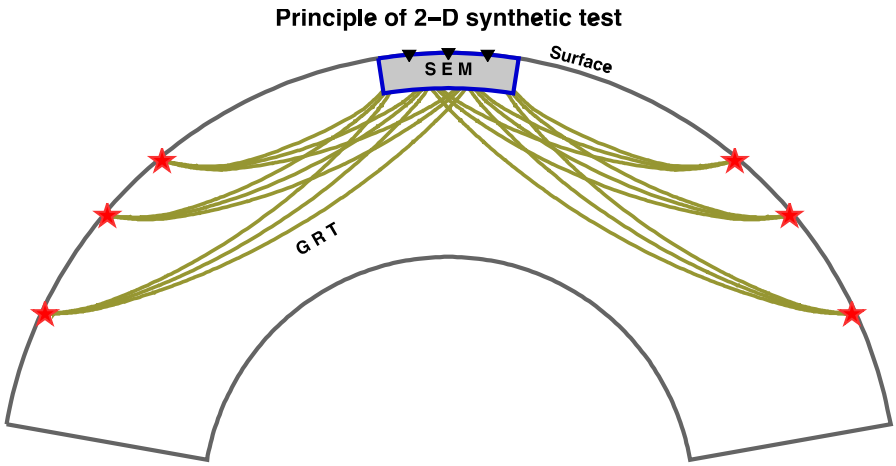


Fig. S5. Basic diagram of the 2-D forward modelling method used in the computation of synthetic seismograms.Triangles denote receivers; stars denote events. SEM: spectral element method; GRT: generalized ray theory.

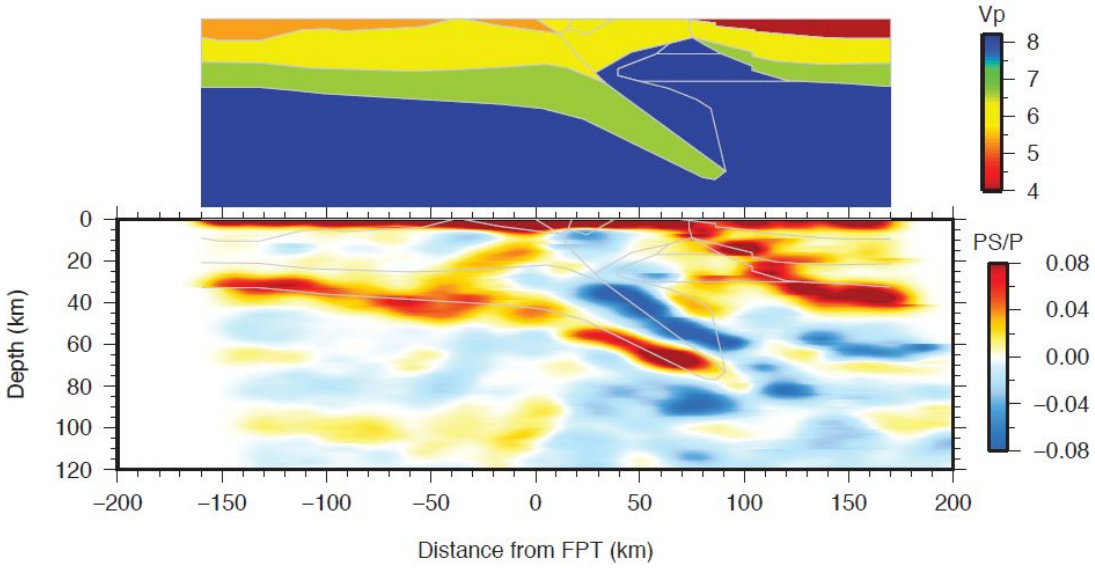


Fig. S6. Synthetic CCP depth section (bottom) computed for a crustal model where a homogeneous mantle wedge (Vp=8.2 km·s$^{-1}$)replaces the Ivrea body and the wedge of UHP metamorphic rocks (top).

## References


25. C. A. Langston, Structure under Mount Rainer, Washington, inferred from teleseismic body waves. J. Geophys. Res. 84, 4749-4762 (1979).

26. J.Ligorría, C. J. Ammon, Iterative deconvolution and receiver-function estimation,Bull. Seismol. Soc. Am. 89, 1395-1400 (1999).

27. L. Zhu, Crustal structure across the San Andreas Fault, southern California from teleseismic converted waves. Earth Planet. Sci. Lett.179, 183-190, (2000).

28. B.L.N.Kennett, E.R. Engdahl,Traveltimes for global earthquake location and phase identification.Geophys. J. Int. 105, 429-465 (1991).

29. Cassidy, J.F., Numerical experiments in broadband receiver function analysis. Bull. Seis. Soc. Am. 82, 1453-1474 (1992).

30. F. Thouvenot, A. Paul,J. Fréchet,N. Béthoux, L. Jenatton, R. Guiguet, Are there really superposed Mohos in the southwestern Alps? New seismic data from fan-profiling reflections, Geophys. J. Int. 170, 1180-1194 (2007).

31. A.Paul, M. Cattaneo, F. Thouvenot, D. Spallarossa, N. Béthoux, J. Fréchet, A three-dimensional crustal velocity model of the southwestern Alps from local earthquake tomography, J. Geophys. Res. 106, 19367–19389 (2001).

32. P. Vernant, F. Masson, R. Bayer, A. Paul, Sequential inversion of local earthquake traveltimes and gravityanomaly—the example of the western Alps, Geophys. J. Int. 150, 79-90 (2002).

33. C.Rangin, X. LePichon, Y.Hamon, N.Loget, A.Crespy, Gravity tectonics in the SE Basin (Provence, France) imaged fromseismic reflection data, Bull. Soc. géol. Fr. 181, 503-530 (2010).

34. I. Molinari, A. Argnani, A. Morelli, P. Basini, Development and testing of a 3D seismic

velocity model of the Po Plain sedimentary basin, Italy. Bull. Seismol. Soc. Am. accepted (2015).

35. M. Talwani, J. L. Worzel, M. Landisman, Rapid gravity computations for two-dimensional bodies with application to the Mendocino submarine fracture zone, J. Geophys. Res. 64, 49-59 (1959).

36. L. Zhao, M. Zhao, G. Lu，Upper mantle seismic anisotropy beneath a convergent boundary: SKS waveform modeling in central Tibet, Science China: Earth Science, 57, 759-776 (2014).

37. L. Zhao, L. Wen, L. Chen, T.Y. Zheng. A two-dimensional hybrid method for modeling seismic wave propagation in anisotropic media. J.Geophys. Res. 113,B12307, doi:10.1029/2008JB005733 (2008).

38. A. Dziewonski , D. Aderson Preliminary reference Earth model. Phys. Earth. Planet. Inter. 25, 297-356 (1981).

39. D. Komatitsch, J. Tromp J., Introduction to the spectral element method for the three-dimensional seismic wave propagation. Geophys J Int, 139, 806-822 (1999).

40. L. Wen, D. Helmberger, A two-dimensional P-SV hybrid method and its application to modeling localized structures near the core-mantle boundary. J. Geophys. Res. 103, 17901-17918 (1998).

41. G. Perrier, J.C.Ruegg, Structure profonde du Massif Central Francais, Ann. Geophys., 29(4), 435－502 (1973).

42. J. Nafe, C. L. Drake, Variation with depth in shallow and deep water marine sediments of porosity, density and the velocities of compressional and shear waves, Geophysics, 22,

523-552 (1957).

43. J.W.Ludwig, J.E. Nafe, C.L. Drake. Seismic refraction, in The Sea, Vol. 4, pp. 53-84, ed. Waxwell, A.E., Willey, New York (1970).

44. N.I. Christensen, Serpentinites, peridotites, and seismology, Int. Geology Rev. 46, 795-816 (2004).